

ORIGINAL ARTICLE

In situ tensile behavior of Hi-Nicalon silicon carbide fibers exposed to high-temperature argon plasma

Zhuang Liu¹  | Jason M. Meyers¹  | Jeffrey Schindler¹ | Frederic Sansoz¹ | Ting Tan²  | Douglas G. Fletcher¹

¹Department of Mechanical Engineering, University of Vermont, Burlington, Vermont, USA

²Department of Civil and Environmental Engineering, University of Vermont, Burlington, Vermont, USA

Correspondence

Jason M. Meyers and Ting Tan, 33 Colchester Ave, Burlington, VT 05405, USA.

Email: jmmeyers@uvm.edu (J. M. M.) and ting.tan@uvm.edu (T. T.)

Funding information

U.S. Navy, Grant/Award Number: Navy SBIR 2019.3-Topic N193-144; NASA EPSCoR, Grant/Award Number: NNX14AN20A; University of Vermont, Grant/Award Number: 028613

Abstract

Direct mechanical characterization of silicon carbide fibers in extreme hypersonic aerothermal environment is critical to the development of next-generation inflatable thermal protection systems that could enable delivery of large payloads to planetary surfaces. In this article, we report direct measurements of tensile properties in Hi-Nicalon silicon carbide fibers exposed to high-temperature argon plasma exceeding 1100°C using an in situ mechanical testing system integrated into a 30-kW inductively coupled plasma torch chamber simulating the hypersonic atmospheric entry conditions. As a comparison, ex situ tensile tests were performed on virgin Hi-Nicalon silicon carbide fibers in both ambient air and vacuum conditions. In situ thermal and optical imaging was used to obtain a real-time resolution of the thermo-mechanical events occurring on the fibers during the high-temperature argon plasma exposure. It is found that the high-temperature tensile strength of Hi-Nicalon fiber tows exposed to argon plasma is 0.74 ± 0.19 GPa, which denotes a 59% reduction from the virgin fiber strength in ambient air (1.81 ± 0.19 GPa). Fractographic characterization by scanning electron microscopy shows that the substantial degradation of tensile strength in Hi-Nicalon fibers results from a reduction of fiber cross-section due to active surface attack from high-temperature argon plasma.

KEYWORDS

degradation, fibers, silicon carbide, strength, thermal properties

1 | INTRODUCTION

The need to accurately deliver larger and heavier payloads to planetary surfaces, which is driven by the desire to land massive human and scientific systems,^{1–4} has called for novel thermal protection system (TPS) strategies that outperform heritage systems. One such promising strategy incorporates a deployable TPS allowing for a larger heat shield geometry to be packed into a limited volume launch platform shroud. Both inflatable^{5–7} and mechanical⁸ systems have been conceived, and these operate on

a similar principle of deploying the heat shield to full diameter early in the entry trajectory. Regardless of system type, these deployable concepts require a flexible woven-fiber fabric to serve as the primary heat mitigation surface. However, there are many aerothermal characteristics related to candidate fiber materials that remain unknown.

Several studies in the literature have been focused on characterizing mechanical properties and failure mechanisms in TPS materials. At room temperature, Sawyer et al.⁹ performed static and cyclic testing on Li-900 RSI tiles, the RTV-560 adhesives, and strain isolator pads (SIP)

under tension and compression. The SIP material exhibited greater tensile strengths with increased displacement rates in static loading, and higher tensile modulus at larger strains in cyclic loading. By conducting three-point bending, Biamino et al.^{10,11} studied mechanical properties in two types of multilayer silicon carbide (SiC) specimens after reentry simulations at thermal and atmospheric loads based on the HERMES trajectory, with maximum temperatures at 1450 or 1550°C. The silicon carbide specimens exhibited a flexural strength of 100 MPa and elastic modulus above 130 GPa. Agrawal et al.¹² performed in situ SEM tensile tests to study the failure mechanisms in phenolic impregnated carbon ablators (PICA), including FiberForm (precursor), virgin and charred PICA ablators. PICA specimens were uniformly charred in a tube furnace to 1300°C within inert environment. Results showed that cracks in FiberForm initiated from interfaces between the carbon fiber and binder, whereas in virgin and charred carbon ablators, cracks initiated and propagated in the phenolic matrix.

The high-temperature tensile strength of SiC fibers has drawn significant interest due to their excellent strength, stiffness, and thermal stability,^{13–19} but studies within the scope of application to flight remain limited.^{20,21} These studies normally made use of a furnace system as heating device and, when oxidation was investigated, only considered material interactions with molecular oxygen from atmospheric air heated from the furnace environment. The Hi-Nicalon fiber is a high-temperature specialty ceramic fiber with β -SiC nanocrystals and stacked carbon layers,²² consisting of Si, C, and O at the ratio of 62:37:0.5 by mass,²³ with less than 0.3% hydrogen inherited from the precursor.²⁰ Yun and Dicarolo²⁴ measured the tensile strength in Hi-Nicalon SiC fibers at room temperature using monofilament and fiber tows in different conditions: As-produced, after exposure at 1000°C for 3 h in vacuum, and after exposure at 1400°C for 1 h in argon. Serizawa et al.²¹ measured the tensile strength of Hi-Nicalon fiber at high temperatures (1100 and 1400°C) by heating fiber specimens in a furnace. Owens et al.²⁰ performed tensile tests at room temperature using Hi-Nicalon woven cloths after being exposed to high-temperature nitrogen and oxygen plasmas. The aero-thermal heating from a 30-kW inductively coupled plasma (ICP) torch was used to simulate the harsh oxidizing environments during hypersonic atmospheric entry, through which Hi-Nicalon woven specimen surfaces reached temperatures over 1400°C with exposure to different high-enthalpy dissociated oxygen, air, and nitrogen plasma flows. Exposure to nitrogen plasma led to moderate strength reduction compared with virgin specimens, whereas exposure to air and oxygen plasmas resulted in severe embrittlement over much shorter time

periods. The formation of a viscous silica surface layer promoted an embrittled layer with different surface defects once the sample was cooled.²⁰ This phenomenon could potentially accelerate fiber failure in the entry trajectory where viscous shear increases with increasing atmospheric density at lower altitudes. To the authors' best knowledge, no data existed on the high-temperature strength of Hi-Nicalon SiC fibers in operando within a ground test facility that has the capability of simulating a realistic hypersonic flow environment.

In this study, we report the in situ tensile strength measurements of Hi-Nicalon SiC fiber exposed to high-temperature argon plasma. The article is structured as follows: First, we describe the development of a mechanical testing system by coupling a 30-kW ICP torch system that is used to simulate the hypersonic atmospheric entry conditions. Second, we present the tensile strength results of Hi-Nicalon fiber specimens exposed to high-temperature argon plasma. For a comparison, room-temperature tensile strengths are measured for virgin fibers in ambient air and vacuum, so as to discern in situ and ex situ mechanical behavior of SiC fibers. Correlated temperature and stress values are collected in real time from in situ stress-temperature measurements. Third, to help reveal the in situ fiber degradation mechanisms, scanning electron microscopy (SEM) images of fractured surfaces are examined to characterize the microstructural changes from tension of Hi-Nicalon fibers exposed to argon plasmas. Finally, the results are discussed with respect to existing data in the literature related to Hi-Nicalon SiC fibers.

2 | MATERIALS AND METHODS

2.1 | 30-kW inductively coupled plasma facility

A 30-kW ICP torch was developed at the University of Vermont to qualify thermal protection system materials and study gas surface interaction physics inherent to the reentry and hypersonic flight environment.²⁵ The plasma jet geometry in this stagnation point heating facility is defined by a 36-mm inner-diameter quartz tube. A radio frequency power supply operating between 2 and 3 MHz is used to generate the plasma via magnetic field coupling in the quartz tube induction zone. Here, plasma temperature is on the order of 10 000 K. The plasma travels vertically upward from the induction zone in the quartz tube toward the sample as a free jet in near local thermodynamic equilibrium. This facility has been operated with pure air, N₂, O₂, CO₂, and argon, as well as admixtures that are widely tailorable. A nominal operating static pressure between 100 and 200 torr ensures laminar

flow and represents post shock pressure of the hypersonic flight environment. Typical stagnation cold wall heat flux values to a 25.4 mm (1.0 in) diameter slug calorimeter range between 10 and 150 W cm⁻² depending on the test condition. Replication of the flight environment is normally achieved when the boundary layer edge velocity gradient, enthalpy, and total pressure of the subsonic ICP match flight values. This facility is normally operated at subsonic conditions but can be configured for supersonic operation.²⁶ A lower power argon plasma was used for this study as a baseline performance check of the in situ tensile test system. This test condition, described in more detail in Section 2.3, was created to get reasonable heat flux to the fiber sample independent of any gas surface interaction effects without incurring thermal failure before tensile tests began. Additional future tests are being considered to test fiber strength sensitivity to gas surface chemistry effects by incorporating nitrogen and oxygen to flow.

2.2 | Development of an in situ mechanical testing system

An in situ mechanical testing system was developed for this study with a control system, load cell, and related data acquisition units, and installed inside the 30-kW ICP torch chamber as schematically shown in Figure 1. Because the plasma jet entered at the bottom center of the chamber, a discrete design was adapted to place the control system and load cell on opposite sides of the chamber.

On the left side of the chamber in Figure 1, a modified TSFM500H stand (Mark-10) with a DC4030 controller (Mark-10) was mounted through a customized stainless steel flange cap. The extended stand provided enough sliding distance so that large tensile/compressive forces could be generated to fracture strong specimens if needed. A 360 brass rod of 9.5 mm in diameter and 394.0 mm in length was supported via a flange-mounted linear sleeve bearing (McMaster-Carr). The left and right ends of the brass rod were mounted to the driver and the brass clamp to hold fiber specimens, respectively.

On the right side of the chamber in Figure 1, a Futek FSH00258 load cell (Futek) was mounted within a customized cylindrical load cell case outside the plasma chamber to maintain a low service temperature. The load cell had a capacity of 2.2 kN in tension/compression. Another brass rod with 9.5 mm in diameter and 135.0 mm in length was used to connect the load cell to the mating clamp via a hole on the cylindrical case, the diameter of which was slightly larger than the rod diameter. The fixed end of the brass rod was connected to the load cell, whereas the free end of the brass rod was connected to the brass clamp holding the other end of fiber specimens. Customized clamps were developed to mount specimens inside the chamber as shown in Figures S1 and S2. The initial distance between the two clamps was 228.6 mm (gauge length), centered over the plasma flow. The applied strain was measured from the elongation of the entire gauge section between the clamps. The system was calibrated for tensile forces ranging from 0 to 889 N. The resulting R^2 value of the linear fitting was equal to 1.0. Multiple sealing strategies were

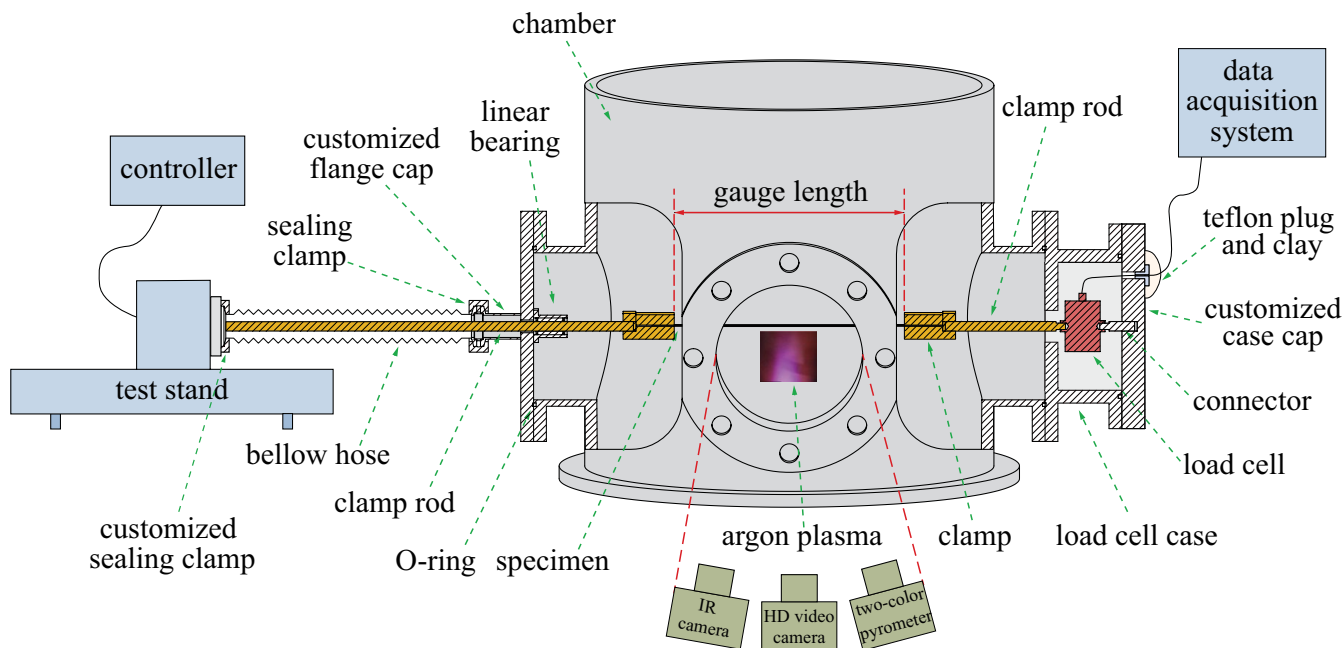


FIGURE 1 Schematics of the in situ mechanical testing system inside the 30-kW plasma chamber

used to ensure vacuum integrity, details of which were included in the Supplementary Materials.

A total of 8 fiber tow specimens were tested exposed to argon plasma at 5.0 mm/min. In situ thermal and optical imaging was conducted with an IR camera (TIM 1M25) (Micro-Epsilon America) and a high-definition digital camera (EOS 7D) (Canon) on the side of fiber specimens, respectively. A two-color Raytek pyrometer (Raytek) was also used to monitor temperature before the IR camera was turned on.

2.3 | Plasma condition during in situ tensile tests

This study only focused on the tensile behavior of fiber exposed to argon plasma. The argon flow rate was 30.0 ± 0.1 SLPM (0.891 ± 0.003 g/s), monitored with MKS flow control hardware. Chamber pressure was maintained constant via a proportional-integral-derivative-controlled bleed valve. A vacuum of 0.8 ± 0.1 torr was achieved prior to the gas introduction. The chamber pressure increased to 160 torr at test condition. Cold wall heat flux to a 25.4-mm diameter copper slug calorimeter for this condition was 5.05 W cm^{-2} . The heat flux was measured 79 mm above the chamber floor where the specimens were located. As stated earlier, the use of argon as the test gas provided high enthalpy heating relevant to an atmospheric entry trajectory while avoiding the thermochemical effects. The temperature for pure argon was about 6000 K representing a flow enthalpy of 3.2 MJ/kg. This corresponded to a flight speed of 2.53 km/s. At altitude, the atmospheric temperature would be about 250 K. The sound speed in argon at that temperature is 294 m/s giving a Mach of 8.6, which is greater than 5 and so the condition represented a hypersonic entry trajectory condition.

2.4 | Ex situ tensile tests

For baseline comparison, two types of ex situ tensile tests were carried out on virgin Hi-Nicalon fiber tows at room temperature with a displacement rate of 5.0 mm/min in ambient air and vacuum conditions, respectively. Seven virgin fiber tow specimens were tested in ambient air, whereas six virgin fiber tow specimens were tested in vacuum. In addition, single-fiber tests were conducted to validate the room temperature tensile strength data published in the literature. Single fibers were tested at the same displacement rate using a Futek LSB200 load cell with tension/compression capacity of 8.9 N (Futek). The

calibration was performed with the force ranging from 0 to 8.9 N. The resulting R^2 value of the linear fitting was equal to 1.0. Load was recorded using a Keysight 34972 data acquisition unit (Keysight) at a sampling rate of 27.8 Hz. Virgin single-fiber specimens were prepared with different gauge lengths of 25.4, 228.6, and 330.2 mm, respectively. Ten tests were duplicated for each single-fiber group.

2.5 | Sample preparation

Hi-Nicalon fibers (COI Ceramics) were used for both in situ and ex situ tensile tests. Fiber tow specimens were prepared using parallel filaments with 147 ± 18 fibers per tow. The diameter of each fiber was $\sim 14 \mu\text{m}$ based on SEM imaging, and the gauge length was 228.6 mm for in situ tensile tests. Rigid specimen ends were created by sandwiching fiber tows between plastic tapes (Totalpack) using a fast-setting epoxy (Henkel). Specimens were cured for 24 h at room temperature before tensile testing. The number of broken fibers in each sample after testing was carefully counted using plano-convex lenses (Newport Optical). The tensile stress σ in the sample was calculated by the equation:

$$\sigma = \frac{F}{n_f \cdot \pi \left(\frac{d}{2}\right)^2} \quad (1)$$

where F is the measured tensile force, n_f is the fiber number in the tow, and d is the fiber diameter.

2.6 | Fractographic characterization

Surfaces of fractured Hi-Nicalon fibers after testing were characterized using a JEOL 6060LV SEM (JEOL USA Inc.). A gold-palladium coating was sputtered onto the surfaces with a thickness of ~ 60 nm.

3 | RESULTS

3.1 | Ex situ tensile testing

Stress-strain curves of the virgin fiber tows tested at room temperature are shown in Figure 2A. Each curve exhibits incremental and sudden-drop load stages. Intermediate failure is detected for some specimens, which is indicative of the early breakage of a portion of fibers in the tow. Figure 2B shows stress-strain curves of fibers tested at room temperature in vacuum (about

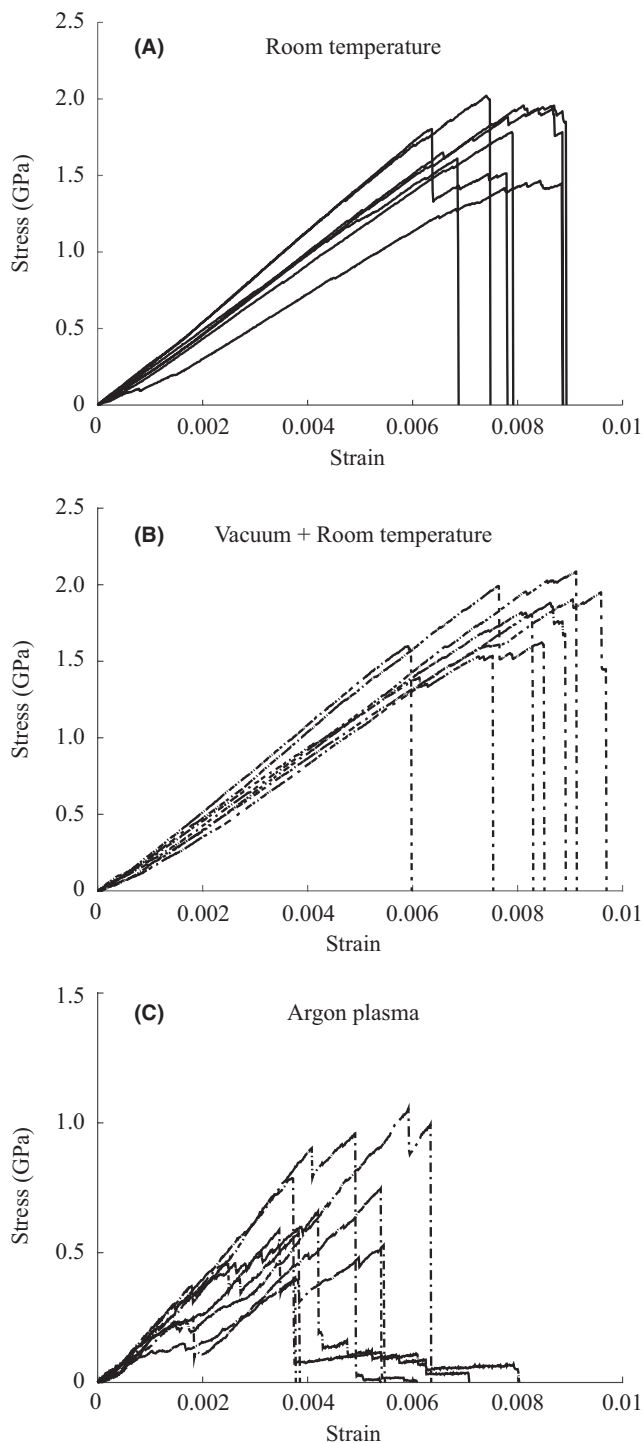


FIGURE 2 Stress-strain curves of virgin fiber tows tested (A) in ambient air at room temperature, (B) in vacuum at room temperature, and (C) during exposure to argon plasma

0.8 torr with no plasma). The curves exhibit similar failure patterns with virgin fibers tested in ambient air. The measured tensile strength of virgin specimens in ambient air is 1.81 ± 0.19 GPa (Figure 3A), whereas the measured tensile strength of virgin specimens in vacuum is 1.84 ± 0.20 GPa. These strength values are comparatively close.

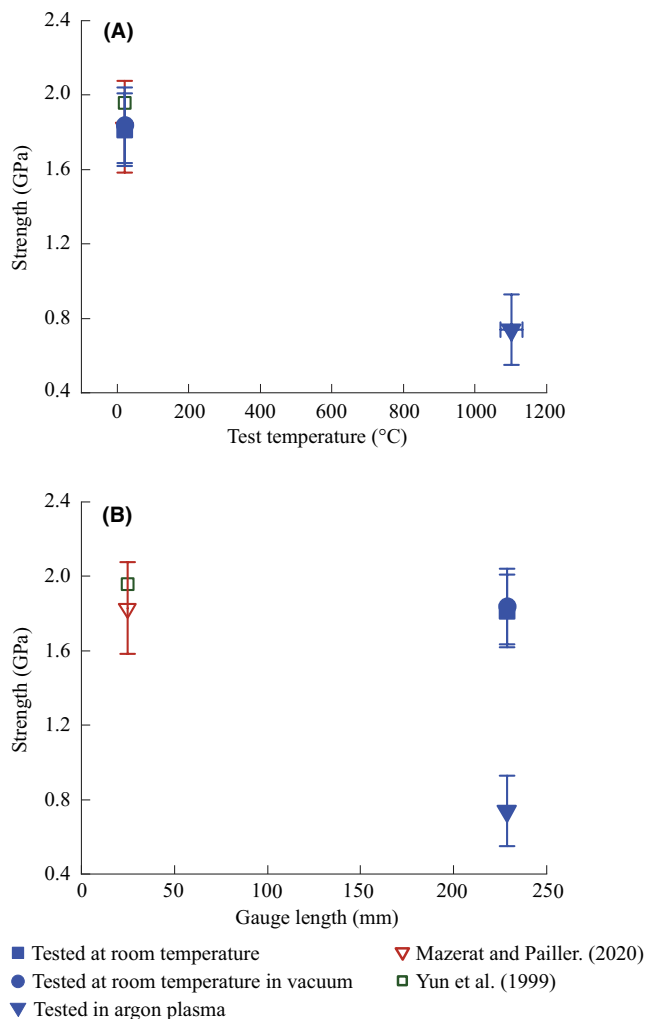


FIGURE 3 Measured tensile strengths of Hi-Nicalon fiber tows at different in situ and ex situ conditions. (A) Average strength versus temperature, (B) average strength versus gauge length. Test temperature is the temperature when the tensile test is conducted. Detailed testing conditions of values in the literature are included in the Supplementary Materials

As shown in Figure 4, the measured tensile strengths vary according to the gauge lengths of single-fiber specimens. When the gauge length is 25.4 mm, the measured tensile strength is 2.77 ± 0.26 GPa, close to the value of 2.8 GPa reported in the literature.^{12,21,27,28} As the gauge length increases, however, the measured tensile strength decreases to 2.53 ± 0.27 and 2.39 ± 0.23 GPa at gauge lengths of 228.6 and 330.2 mm, respectively. This finding suggests that surface or volume defects^{29,30} play a key role in the tensile strength limit and brittle behavior of Hi-Nicalon fibers. Preliminary Weibull analysis of Hi-Nicalon fiber tow and monofilament is included in Figures S3 and S4. Furthermore, a good agreement is found for the measured strengths from fiber tows and monofilaments tested at room temperature when compared with reported data in the literature^{19,20,24,31,32} in Figures 3A,B and 4A,B, respectively.

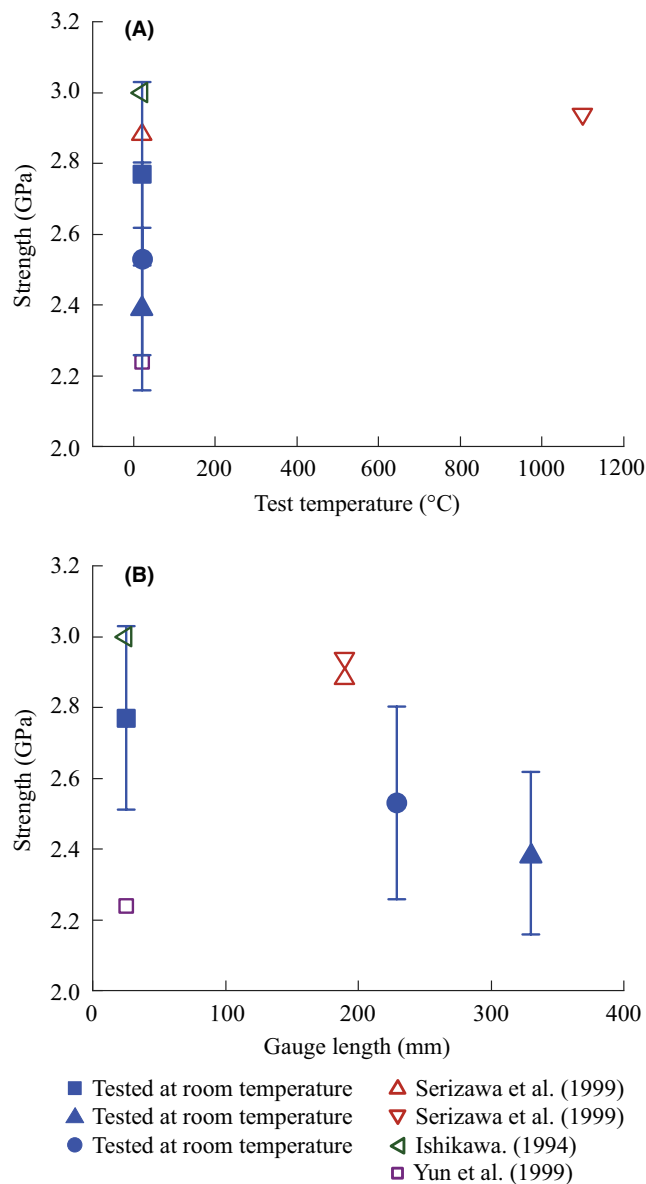


FIGURE 4 Measured tensile strengths of Hi-Nicalon fibers using monofilament at different in situ and ex situ conditions. (A) Average strength versus temperature, (B) average strength versus gauge length. Detailed testing conditions of values in the literature are included in the Supplementary Materials

3.2 | In situ tensile testing

The data in this section represent results from in situ tests in the ICP facility. The in situ stress-strain curves of fibers exposed to argon plasma are shown in Figure 2C. The curves in this figure exhibit more local stress drops during the initial loading compared with those from ex situ tests (Figure 2A,B). This may be related to the coupled local heat and the dynamic movement of fibers resulting from the blast of argon plasma. At later stage of deformation, we can identify that two types of decrease stages occur: sudden drops and the extended stepwise failure. This observation

suggests that the fiber tows encounter different breaking stages, which is further discussed below. When exposed to argon plasma, the measured tensile strength of Hi-Nicalon fibers is found to be 0.74 ± 0.19 GPa (Figure 3C), which indicates that, while the argon plasma resulted in at least 50% decrease in tensile strength, the statistical strength variation did not change compared with that of virgin fibers tested ex situ. In this study, all ex situ specimens failed between mounted ends, whereas all in situ specimens failed at the segments exposed to high-temperature argon plasmas. These results confirmed that the mounted ends were successful in holding specimens during tests.

3.3 | In situ optical and thermal imaging

We now pay attention to the details of the real-time optical and thermal analysis during stretching of Hi-Nicalon fibers exposed to argon plasma. Snapshots of a representative specimen at different stages of elongation are presented in Figure 5A–D, along with the temperature contours shown in Figure 5E–H, respectively. In this figure, the parameter t_f denotes the time for the stress to drop at the peak of the stress-strain curve. In the beginning ($t = 0$), the purple jet of argon plasma is turned on, covering the fiber section in the middle (Figure 5A). The thermal contours show that the highest temperature occurs in the fiber section directly exposed to argon plasma, and the temperature quickly decreases from the central section to the surrounding space.

As the test continues to evolve, the temperature inside the chamber increases. Where the central fiber section is highlighted ($t = 0.5t_f$), a small number of SiC fibers fail as tension is applied, whereas most of the parallel fibers remain unbroken. We attribute this behavior to the progressive failure of fibers starting from those most exposed to argon plasma. The unbroken fibers remained stable during tension, whereas the broken fibers that are quickly vibrating illustrate the strong driving force resulting from the plasma jet (Figure 5B). Thermal contours in Figure 5F reveal the substantial difference between the higher temperature in the fiber segment exposed to argon plasma and lower temperature for sections away from the plasma jet.

At the point of complete specimen failure ($t = t_f$), broken fiber segments fly violently up the plasma jet (Figure 5C), whereas limited fiber segments exposed to the plasma jet remain intact. The suddenly broken fibers clearly confirm the catastrophic tensile failure of Hi-Nicalon fibers exposed to high-temperature argon plasma, which are consistent with the sudden stress drops illustrated in Figure 2C. In contrast to relatively steady contours shown in Figure 5A,B, large thermal fluctuations exist within the central region, whereas the temperature decreases rapidly away from the center (Figure 5G).

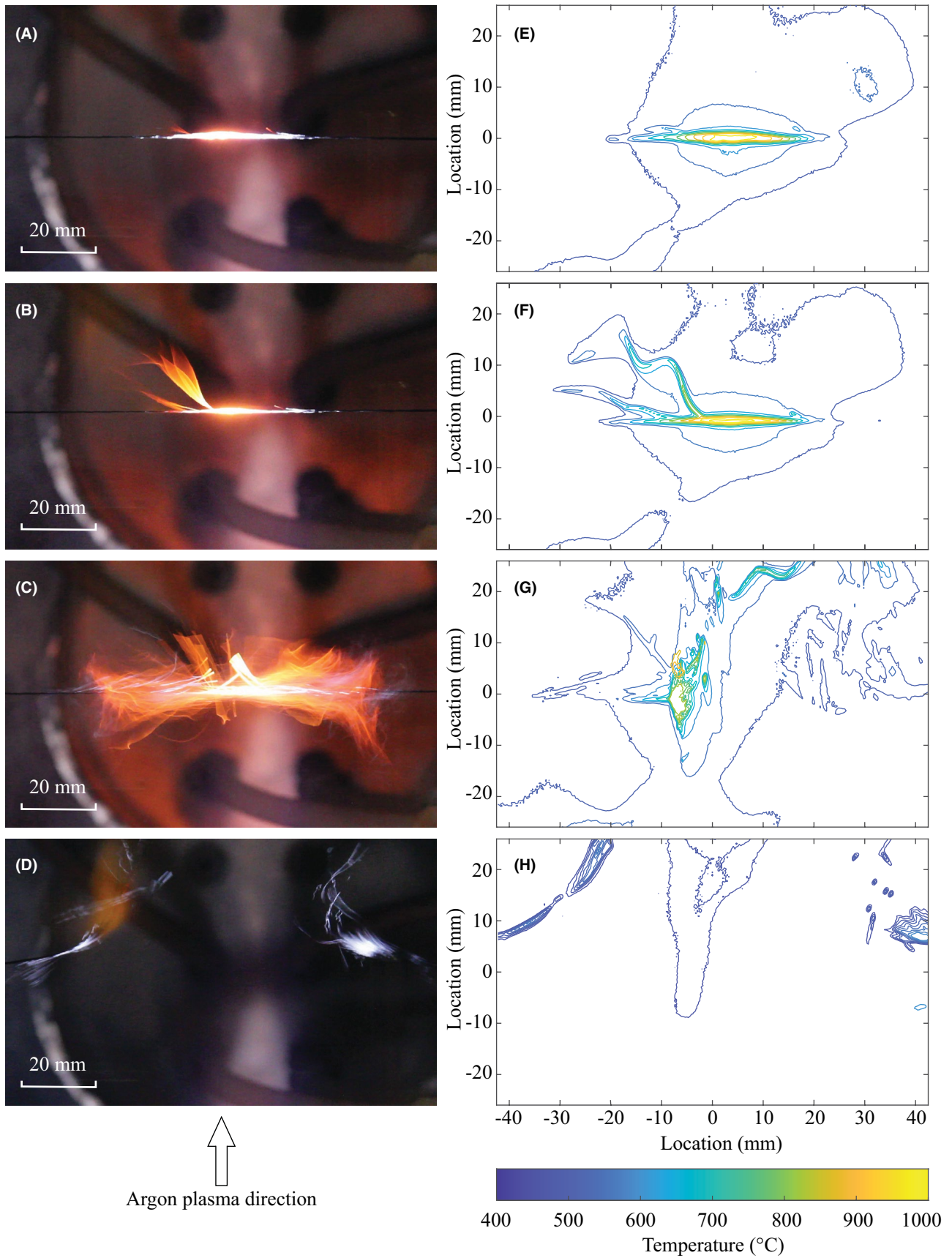


FIGURE 5 (A–D) Optical snapshots of fiber specimen under tension at $t = 0$, $0.5t_f$, t_f and $1.2t_f$. (E–H) 2D snapshots of temperature contours at $t = 0$, $0.5t_f$, t_f and $1.2t_f$. The origin of the camera window locates at (0, 0) of contours with a size of 51.9 mm by 85.0 mm. The direction of argon plasma is marked by the arrow

After the fiber breakage ($t = 1.2t_f$), two separated fiber segments fly to opposite sides of the plasma jet (Figure 5D). Because no intact fibers are exposed to the plasma jet, the thermal contour (Figure 5H) is different from prior contours (Figure 5E–G). Relatively uniform thermal contours existed among the observed area. This is probably because the observed contours primarily reflect the temperature distribution induced by the argon plasma.

The temperature evolution along the central line of the observed area is shown in Figure 6. The average temperatures along the central fiber segment are plotted for all fiber specimens at $t = 0$, $0.5t_f$, t_f and $1.2t_f$, and standard deviations of temperature are added accordingly. It shows that the temperature profiles first increase from $t = 0$ to the moment of major fiber fracture ($t = t_f$), then decrease after the fiber failure ($t = 1.2t_f$). At $t = 0$, large standard deviations of temperature are measured because of the quickly changing thermal status. As the test continues, smaller standard deviations are reported before the fiber breakage ($t = 0.5t_f$ and $1.0t_f$) suggesting that intact fibers under tension exhibit stable high-temperature spots when exposed to argon plasma. After failure ($t = 1.2t_f$), standard deviations become larger again owing to the highly transient thermal field above the argon plasma jet. Thus, the temperature at the central segment first increases from the beginning to the moment of fracture, and then decreases after the fiber breakage. A video recording the in situ tensile test is included in the Supplementary Materials.

3.4 | Thermo-mechanical history during in situ tensile testing

The time evolutions of temperature and stress in Hi-Nicalon fibers during in situ tests exposed to argon plasma are plotted in Figure 7. The temperature evolutions over the scaled durations are plotted at the location (0 mm)

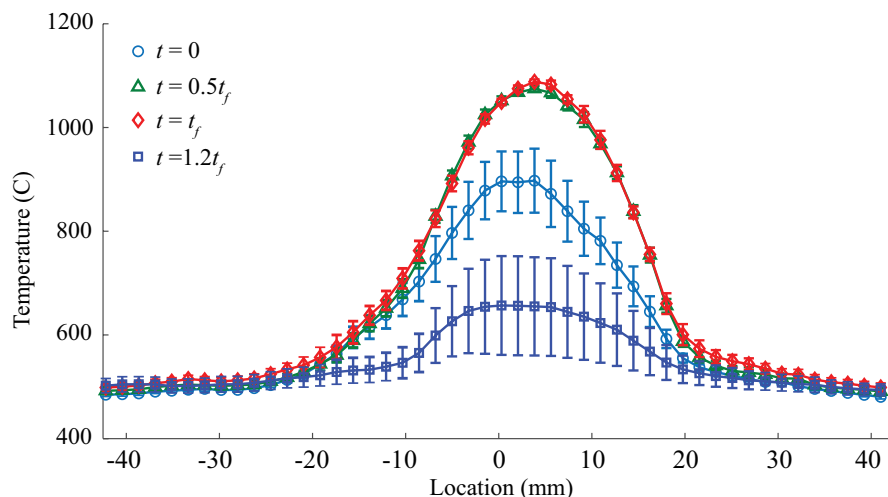


FIGURE 6 Averaged temperature profiles along the central axis of samples at $t = 0$, $0.5t_f$, t_f and $1.2t_f$

of the monitor window as illustrated in Figure 7. The maximum temperatures of the monitor window sized at 51.9 mm by 85.0 mm are plotted in red over the test duration, whereas the average temperature of a smaller central window sized at 32.5 mm by 17.7 mm are plotted in green to represent the temperature within the plasma heated fiber section. Two types of thermo-mechanical histories are observed during in situ tests. For the first type, the temperature slightly increases from the beginning of tests to the moment of fiber fracture (Figure 7A). Subsequently, the temperature drops suddenly because broken fiber tows fly to the opposite sides of the plasma jet (Figure 7B). However, the second type exhibits a slightly increased temperature after the major fiber breakage (Figure 7D) because some broken fibers are entangled with each other after breakage (Figure 7C). The partial bonding between broken fibers that are not blown away by the plasma jet serve as sites on which the measured temperatures continue to increase.

Among the eight fiber specimens of in situ tests, we found that six specimens exhibited the first type of thermo-mechanical behavior, with only two for the second behavior. Figure 8 where all thermal histories are plotted over the scaled durations shows that specimens with similar thermo-mechanical histories can be collapsed together. A consistent trend is found: the temperature drops immediately at the major fiber breakage for specimen broken into halves, whereas temperature increases slightly for specimens entangled after the major fiber fracture.

3.5 | Fractographic characterization

SEM images of the fractured surfaces of individual fiber samples tested under different conditions are shown in Figure 9. This figure shows two distinctive features between in situ (Figure 9A,B) and ex situ specimens (Figure

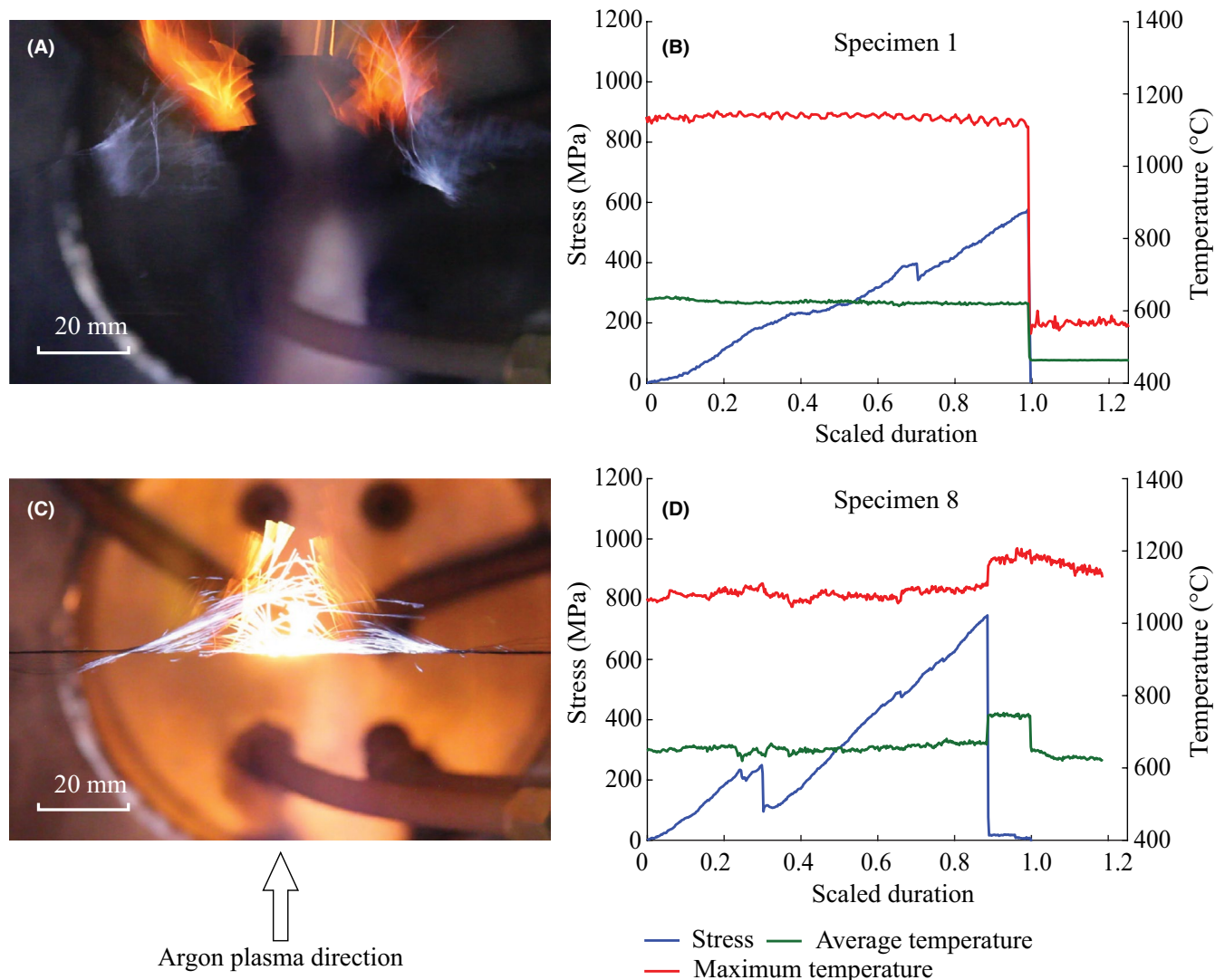


FIGURE 7 Thermo-mechanical time evolution during in situ tensile tests. (A, C) The observed fiber tows after the major fiber fracture. (B, D) Stress and temperature histories over the scaled duration of Hi-Nicalon fibers during in situ tensile tests. The direction of argon plasma is denoted by the arrow. The maximum temperature is obtained from the window sized at 51.9 mm by 85.0 mm, whereas the average temperature is obtained from the window focusing on the central fiber section sized at 32.5 mm by 17.7 mm

9C,D). First, we find that the fracture zone of the etched cylindrical fibers (less than 5% in tows) exhibits substantially reduced segments (curved shapes pointed by arrows in Figure 9A,B) $\sim 8\text{--}10\ \mu\text{m}$ in width in Figure 9A,B when most exposed to high-temperature argon plasma, compared to $\sim 13\text{--}17\ \mu\text{m}$ in diameter in Figure 9C,D with ex situ tests. This observation suggests that the surfaces of some horizontal SiC fibers were attacked by the vertical plasma jet sideways. Figure 9A exhibits a tilted fracture surface of an etched fiber, which is different from the significantly flatter surfaces shown in ex situ tests in Figure 9C,D. This phenomenon could be indicative of the etched segment geometry affects the stress concentration in fibers, that is, the reduced fiber regions serve as stress concentrators. Furthermore, other reasons may also affect the failure, such as a change of loading

mode induced by the large-amplitude oscillations of the fiber inside the plasma jet evidenced in Figures 5 and 7. Potential oxygen contamination in our argon flow comes from two sources: argon gas bottle impurities and level of vacuum base pressure before testing. The argon gas used was of ultra-high-pure grade from Airgas,³³ which has a purity of 99.999% with at most 20% of that contaminant being oxygen from air. This would provide an oxygen percent in plasma flow due to argon gas bottle impurities at $\sim 0.0002\%$. Base pressure of our facility before testing was 0.8 torr, and all tests were operated at 160 torr, implying that 0.5% air was in the chamber. By assuming 20% of air was O_2 and 0.5 diffusion efficiency to the center of the jet, there is $\sim 0.05\%$ O_2 in the jet. The trace air could have an effect on the material performance of fibers in the experiments.

4 | DISCUSSION

For ex situ tests, the measured tensile strength from virgin Hi-Nicalon fiber tows tested at room temperature at atmospheric pressure (1.81 ± 0.19 GPa) is close to the tensile strength from virgin fiber tows tested in vacuum at room temperature (1.84 ± 0.20 GPa), between which the difference is only 1.3%. The tensile strength (2.77 ± 0.26 GPa) measured by monofilament tests with the gauge length of 25.4 mm agrees with reported value in the literature (2.8 GPa), which also validates the

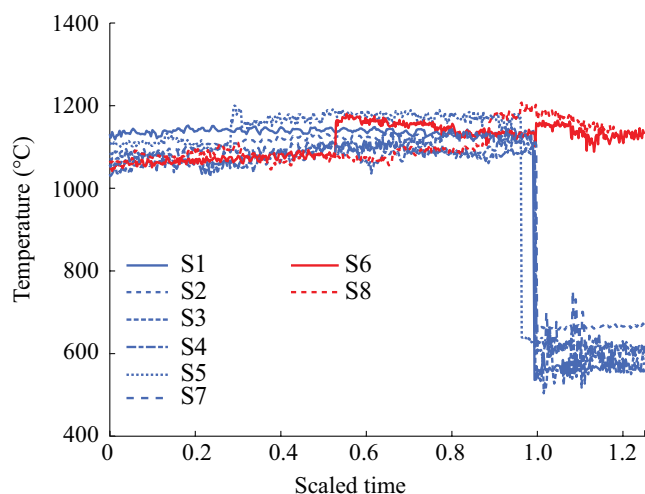


FIGURE 8 Overlapped histories of maximum temperature for in situ fiber specimens over scaled test durations. S1 to S8 represents specimens 1 to 8 exposed to high-temperature argon plasma

performance of the developed experimental systems in this study. In this study, all measured average strengths are larger than the standard deviation, and the standard deviations are similar to values in corresponding conditions reported in the literature. In this study, this effect is manifested by the relatively large statistical distribution of tensile strengths of the fibers in the tows that did not fail all at once, but rather gradually as shown in the stress-strain curves in Figure 2. The calculated Weibull modulus of fiber strength at room temperature with sample sizes (7–10) range between 10 and 12, which are higher than the Weibull modulus (4–10) in the literature with sample sizes (30–50).^{32,34–36} This agrees with prior finding that the Weibull modulus is mostly overestimated for small sample size.^{37,38} We will collect more data in the future to further determine the Weibull modulus at in situ and ex situ conditions. The measured tensile strength decreases as the gauge length increases, consistent with prior findings.^{12,21,39} Furthermore, at room temperature, the measured tensile strength from fiber tows (1.81 ± 0.19 GPa) is lower than that of single fibers (2.53 ± 0.27 GPa) with the same gauge length, indicating that fiber tows exhibit lower strength than individual filaments due to different factors, such as fiber bundle effect accounting for the statistical distribution of filament strengths in a fiber bundle, the friction and dynamic coupling associated with release waves.^{40–43}

For in situ tests exposed to high-temperature argon plasma, the measured tensile strength of Hi-Nicalon fiber tows is 0.74 ± 0.19 GPa, which is reduced by 59% with respect to the tensile strength of virgin fiber tows tested in ambient air (1.81 ± 0.19 GPa). This softening effect is

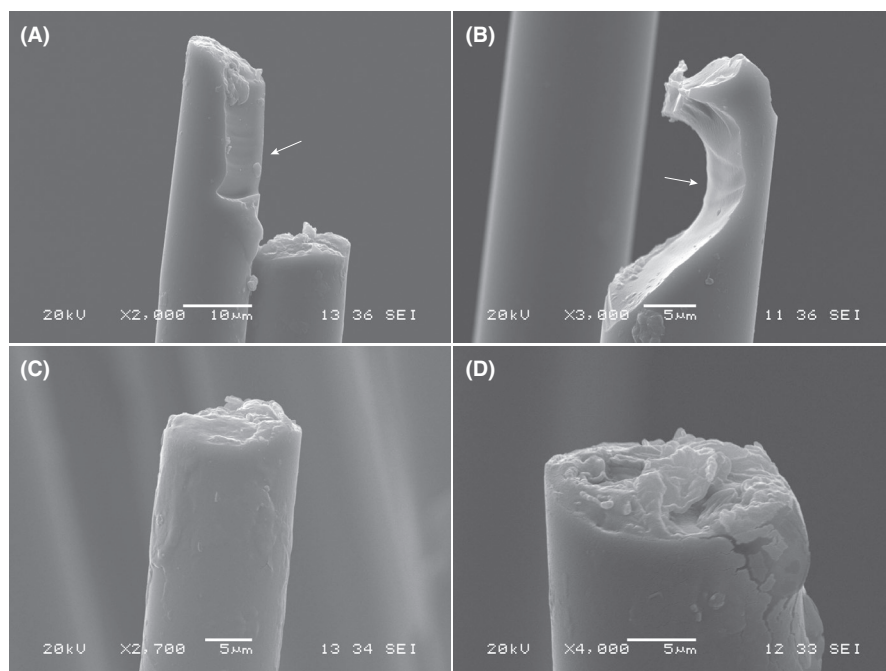


FIGURE 9 SEM images of fractured Hi-Nicalon fibers tested under different conditions. (A, B) in situ tests of fibers exposed to high-temperature argon plasma. (C, D) Ex situ tests of virgin fibers at room temperature

attributed to the distinctive failure mechanisms between in situ and ex situ specimens which are revealed by post-mortem characterization of fracture specimens in Figure 9. As shown in Figure 9, in situ fiber specimens exposed to high-temperature argon plasma exhibited some regions of substantially reduced cross-section that did not appear with virgin specimens tested at room temperature. This change could act as local stress concentrations reducing the overall fiber strength with argon plasma. While high-purity argon plasma should be considered inert, active oxidation resulting from trace amounts of oxygen in argon has been shown to contribute to the accelerated failure of SiC fibers from a similar phenomenon.²⁰ The active oxidation resulting from the small amount of oxygen may contribute to the failure of SiC fibers in this study. These essential defects on SiC fibers significantly decrease the tensile strengths represented in Figure 2. In this study, the fiber specimens are perpendicular to the plasma direction, which may lead to the report of relatively lower strength of the fiber. Future work could be performed to clarify the relationship between fiber strengths and different plasma orientations. For ex situ specimens in ambient air, virgin fibers exhibit relatively flat fracture surfaces with small and irregular pieces (Figure 9C,D). This is consistent with the observation of ceramic fracture under tension, which shows brittle fracture occurring on the planes with maximum normal stress.

in situ thermo-mechanical events are also elucidated in this study by using thermal and optical imaging techniques. Temperature on the fiber segment exposed to argon plasma increases slightly from the beginning to the moment of major fiber fracture. If fiber tows are separated completely, the measured temperature drops suddenly after breakage and the chamber temperature is primarily affected by the argon plasma afterwards. If fiber tows are partially tangled after breakage, the temperature slightly increases after the major breakage because these entangled segments serve as hot spots with high temperature. Therefore, our in situ imaging reveals the existence of more complex and harsher thermo-mechanical conditions in those local fiber regions than the conditions typically encountered in static furnace heating, which can help better understand the accelerated failure mechanisms in flexible SiC materials subjected to high-temperature hypersonic plasma environments.

5 | CONCLUSIONS

This work presented the development of an in situ mechanical testing system inside a 30-kW inductively plasma torch chamber used to simulate the hypersonic atmospheric entry conditions. Multiple strategies were adapted

to ensure the integrity between the loading system and vacuum condition. The demonstration focused on the in situ tensile testing of Hi-Nicalon fibers exposed to high-temperature argon plasma. The in situ tensile strength of Hi-Nicalon fiber tows exposed to high-temperature argon plasma was found equal to 0.74 ± 0.19 GPa, significantly lower than the ex situ tensile strength of virgin fiber tows measured in ambient air (1.81 ± 0.19 GPa). The difference in tensile strength was attributed to the distinctive failure mechanisms between in situ and ex situ fiber specimens. Cross-sections of in situ specimens are substantially reduced by the attack from high-temperature argon plasma, resulting in a lower tensile force at break. Furthermore, local temperature in the fracture region exposed to argon plasma was found to increase from the beginning of tensile tests to the moment of major fiber fracture. The temperature drops suddenly if fiber tows are separated completely after breakage. Otherwise, the temperature increases slightly after the major breakage as the entangled segments initiate hot spots. This work provides insights into the performance of SiC fibers under the simulated hypersonic atmospheric entry condition. The proposed experiment could pave new avenues to precisely characterize the mechanical performance of woven ceramic fibers, ceramic fiber composites, and other high-temperature ceramic materials subjected to different monotonic or cyclic loadings under atmospheric entry conditions.

ACKNOWLEDGMENTS

This work was supported by NASA EPSCoR [grant number NNX14AN20A, Dr. Anthony Calamino, technical monitor; Navy SBIR 2019.3-Topic N193-144: Innovative, Affordable Testing Methodologies for Hypersonic Vehicle Material Systems (Dr. Anant Singh, Triton Systems, technical monitor); University of Vermont (UVM) clean energy fund grant number 028613], and College of Engineering and Mathematical Sciences at UVM. We are grateful Dr. Anthony Calamino at NASA Langley Research Center for providing the Hi-Nicalon fibers. We thank Floyd Vilmont in Mechanical Engineering of UVM for customizing structural components of the system. We appreciate Paul Decausemacker at Art and Art History of UVM for building the full-scale wood test stand. We acknowledge efforts from Professor Darren Hitt, Professor Dryver Huston, and Professor Yves Dubief to the project. Appreciation is also extended to Michele von Turkovich in the UVM Microscopy Imaging Center for her assistance in microscopic characterization.

ORCID

Zhuang Liu  <https://orcid.org/0000-0002-7567-8938>

Jason M. Meyers  <https://orcid.org/0000-0001-8078-9774>

Ting Tan  <https://orcid.org/0000-0002-0847-2542>

REFERENCES

- Hash D, Venkatapathy R, Wercinski P, Ellerby D, Wright M, Cassell A. Presentation to technology. Innovation & Engineering Committee NASA Advisory Council. 2018.
- Wright M, Barnhardt M, Hughes M. Current investments in the NASA. Entry Systems Modeling Project. 2017.
- Wright MJ. Space technology mission directorate game changing development program. 2018.
- Hughes S, Ware J, Del Corso J, Lugo R. Deployable aeroshell flexible thermal protection system testing. 20th AIAA Aerodynamic Decelerator Systems Technology Conference and Seminar; 2009.
- DiNonno J, Cheatwood F, Hughes S, Ragab M, Dillman R, Bodkin R, et al. HIAD on ULA (HULA) orbital reentry flight experiment concept. 2016.
- Del Corso J, Cheatwood F, Bruce W, Hughes S, Calomino A. Advanced high-temperature flexible TPS for inflatable aerodynamic decelerators. 21st AIAA Aerodynamic Decelerator Systems Technology Conference and Seminar; 2011.
- Okeefe S, Bose D, editors. IRVE-II post-flight trajectory reconstruction. AIAA Atmospheric Flight Mechanics Conference; 2010.
- Venkatapathy E, Hamm K, Fernandez I, Arnold J, Kinney D, Laub B, et al. Adaptive deployable entry and placement technology (ADEPT): a feasibility study for human missions to Mars. 21st AIAA Aerodynamic Decelerator Systems Technology Conference and Seminar; 2011.
- Sawyer JW, Rummeler DR. Room temperature mechanical properties of shuttle thermal protection system materials. 1980.
- Biamino S, Antonini A, Eisenmenger-Sittner C, Fuso L, Pavese M, Fino P, et al. Multilayer SiC for thermal protection system of space vehicles with decreased thermal conductivity through the thickness. *J Eur Ceram Soc.* 2010;30(8):1833–40.
- Biamino S, Liedtke V, Badini C, Euchberger G, Huertas Olivares I, Pavese M, et al. Multilayer SiC for thermal protection system of space vehicles: manufacturing and testing under simulated re-entry conditions. *J Eur Ceram Soc.* 2008;28(14):2791–800.
- Agrawal P, Chavez-Garcia JF, Pham J. Fracture in phenolic impregnated carbon ablator. *J Spacecr Rockets.* 2013;50(4):735–41.
- Bodet R, Bourrat X, Lamont J, Naslain R. Tensile creep behaviour of a silicon carbide-based fibre with a low oxygen content. *J Mater Sci.* 1995;30(3):661–77.
- DiCarlo JA, Dutta S. Continuous ceramic fibers for ceramic matrix composites. West Lafayette, IN: Purdue University; 1995, p. 137–83.
- Kumagawa K, Yamaoka H, Shibuya M, Yamamura T. Fabrication and mechanical properties of new improved Si-M-C(O) Tyranno fiber. In: Bray D, editor. 22nd annual conference on composites, advanced ceramics, materials, and structures: A: ceramic engineering and science proceedings. Westerville, OH: Wiley Online Library; 1988. p. 65–72.
- Okamura K. Ceramic fibres from polymer precursors. *Composites.* 1987;18(2):107–20.
- Penide-Fernandez R, Sansoz F. Microscale Knudsen effect over the transverse thermal conductivity of woven ceramic fabrics under compression. *Int J Heat Mass Transfer.* 2021;171:121085.
- Takeda M, Sakamoto J, Imai Y, Ichikawa H, Ishikawa T. Properties of stoichiometric silicon carbide fiber derived from polycarbosilane. In: Wachtman Jr. JB, editor. Proceedings of the 18th annual conference on composites and advanced ceramic materials—A: ceramic engineering and science proceedings. Westerville, OH: Wiley Online Library; 1994. p. 133–41.
- Yun HM, DiCarlo JA. High temperature contraction behavior of polymer-derived SiC fibers. *Ceramic Engineering and Science Proceedings;* 1997.
- Owens W, Merkel D, Sansoz F, Fletcher D. Fracture behavior of woven silicon carbide fibers exposed to high-temperature nitrogen and oxygen plasmas. *J Am Ceram Soc.* 2015;98(12):4003–9.
- Serizawa H, Lewinsohn C, Youngblood G, Jones R, Johnston D, Kohyama A. Evaluation of advanced SiC fibers for reinforcement of CMC. *ICCM-12 Eur Proc.* 1999;1:378–87.
- Chollon G, Pailler R, Naslain R, Laanani F, Monthieux M, Olry P. Thermal stability of a PCS-derived SiC fibre with a low oxygen content (Hi-Nicalon). *J Mater Sci.* 1997;32(2):327–47.
- COI Ceramics I. Hi-Nicalon ceramic fiber. <https://pdf4pro.com/cdn/hi-nicalon-ceramic-fiber-59597b.pdf>. Accessed on July 31, 2021.
- Yun HM, DiCarlo JA. Thermomechanical characterization of SiC fiber tows and implications for CMC. 1999.
- Owens W, Uhl J, Dougherty M, Lutz A, Fletcher D, Meyers J, editors. Development of a 30kw inductively coupled plasma torch for aerospace material testing. In: 10th AIAA/ASME Joint Thermophysics and Heat Transfer Conference. Chicago, IL: AIAA; 2010. p. 1–15.
- Smith S. Investigation of subsonic and supersonic flow characteristics of an inductively coupled plasma facility. 2013.
- Suib SL. A review of nanoceramic materials for use in ceramic matrix composites. In: Mishra AK, editor. Sol-gel based nanoceramic materials: preparation. Properties and applications. Cham, Switzerland: Springer; 2017. p. 185–230.
- National Research Council. Ceramic fibers and coatings: advanced materials for the twenty-first century. Washington, D.C.: National Academies Press; 1998.
- Hay RS, Chater RJ. Oxidation kinetics strength of Hi-NicalonTM-S SiC fiber after oxidation in dry and wet air. *J Am Ceram Soc.* 2017;100(9):4110–30.
- Hay RS, Robertson SJ, Ruggles-Wrenn MB, Piper M, Shillig T, Mitchell R, et al. Subcritical crack growth models for static fatigue of Hi-NicalonTM-S SiC fiber in air and steam. *J Am Ceram Soc.* 2021;104(7):3562–92.
- Ishikawa T. Recent developments of the SiC fiber Nicalon and its composites, including properties of the SiC fiber Hi-Nicalon for ultra-high temperature. *Compos Sci Technol.* 1994;51(2):135–44.
- Mazerat S, Pailler R. Statistical data for the tensile properties and static fatigue of sic-based tows. *Data Brief.* 2020;32:106166.
- Airgas Product Catalog. Pure Gasses, Argon. <http://airgasscatalog.com/catalog/>. Accessed on July 31, 2021.
- Morimoto T, Ogasawara T. Potential strength of Nicalon™, Hi Nicalon™, and Hi Nicalon Type S™ monofilaments of variable diameters. *Compos A.* 2006;37(3):405–12.
- Sha J, Nozawa T, Park J, Katoh Y, Kohyama A. Effect of heat treatment on the tensile strength and creep resistance of advanced SiC fibers. *J Nucl Mater.* 2004;329:592–6.
- Youngblood GE, Lewinsohn C, Jones RH, Kohyama A. Tensile strength and fracture surface characterization of Hi-Nicalon™ SiC fibers. *J Nucl Mater.* 2001;289(1–2):1–9.
- Danzer R, Supancic P, Pascual J, Lube T. Fracture statistics of ceramics—Weibull statistics and deviations from Weibull statistics. *Eng Fract Mech.* 2007;74(18):2919–32.

38. Nohut S. Influence of sample size on strength distribution of advanced ceramics. *Ceram Int*. 2014;40(3):4285–95.
39. Vautard F, Dentzer J, Nardin M, Schultz J, Defoort B. Influence of surface defects on the tensile strength of carbon fibers. *Appl Surf Sci*. 2014;322:185–93.
40. Callaway EB, Zok FW. Strengths of ceramic fiber bundles: Theory and practice. *J Am Ceram Soc*. 2017;100(11):5306–17.
41. Hay RS. SiC fiber strength after low pO₂ oxidation. *J Am Ceram Soc*. 2018;101:831–44.
42. Phoenix SL. Probabilistic strength analysis of fibre bundle structures. *Fibre Sci Technol*. 1974;7(1):15–31.
43. Languerand D, Zhang H, Murthy N, Ramesh K, Sansoz F. Inelastic behavior and fracture of high modulus polymeric fiber bundles at high strain-rates. *Mater Sci Eng A*. 2009;500(1–2):216–24.

SUPPORTING INFORMATION

Additional supporting information may be found online in the Supporting Information section.

How to cite this article: Liu Z, Meyers JM, Schindler J, Sansoz F, Tan T, Fletcher DG. In situ tensile behavior of Hi-Nicalon silicon carbide fibers exposed to high-temperature argon plasma. *J Am Ceram Soc*. 2021;00:1–13. <https://doi.org/10.1111/jace.18073>